Defect spectroscopy and non-ionizing energy loss analysis of proton and electron irradiated p-type GaAs solar cells

C. Pellegrino,[1,2,a)] A. Gagliardi,[2,b)] and C. G. Zimmermann[1,c)]

AFFILIATIONS

[1]Airbus Defence and Space GmbH, 82024 Taufkirchen, Germany
[2]Institute for Nanoelectronics, Technical University of Munich, 80333 Munich, Germany

[a)]Electronic mail: carmine.pellegrino@tum.de
[b)]Electronic mail: alessio.gagliardi@tum.de
[c)]Author to whom correspondence should be addressed: claus.zimmermann@airbus.com

ABSTRACT

Admittance spectroscopy combined with non-ionizing energy loss (NIEL) analysis is shown to be a powerful tool for analyzing solar cell radiation degradation, not relying on the change of macroscopic cell parameters. GaAs component cells, representative of the middle sub-cell in $Ga_{0.5}In_{0.5}P/GaAs/Ge$ solar cells, were irradiated with protons and electrons in the 0.5–3 MeV energy range. Four irradiation-induced defects are identified in the p-type base layer. The nature of each defect is assessed by analyzing the dependence of its introduction rate on the NIEL deposited by electrons in the semiconductor. The expected linear relationship is only achieved if a unique threshold energy E_d is ascribed to each defect, which ranges from 9 to 38 eV. An electron NIEL with $E_d = 21$ eV, customarily used for GaAs-based solar cell degradation analysis, is an approximation of the relative abundance of these four defects. The 21 eV value is thus a GaAs material-specific parameter, independent of the electrical device design. In addition, the type and energy of the incident particle is correlated with the relative abundance of high E_d defects. The impact of each defect on the macroscopic electrical parameters of the cell, namely, the open-circuit voltage V_{OC}, the short-circuit current density J_{SC}, and the recombination current density J_{02}, is assessed with the help of a Pearson analysis. The different effectiveness of electron and proton irradiation on parameters dominated by recombination in the depleted region, such as V_{OC} or J_{02}, is attributed in part to the influence of the particle recoil spectra on the defect capture cross section.

I. INTRODUCTION

Solar cells operated in space are subjected to proton and electron irradiation in the MeV energy range, which generates displacements in the lattice via elastic collisions with crystal atoms. In $Ga_{0.5}In_{0.5}P/GaAs/Ge$ triple-junction solar cells, the GaAs sub-cell is mostly electrically degraded by this non-ionizing damage and is thus the most interesting one to analyze. The number of displacements generated in GaAs by a particle spectrum characterized by a differential fluence $\phi(\xi)$ can be computed via the displacement damage dose $(DDD) = \int_\xi NIEL(\xi)\phi(\xi)\,d\xi$, where ξ denotes the particle energy. The non-ionizing energy loss (NIEL) quantifies the amount of non-ionizing damage that the primary particle and all its recoils deposit in the lattice in the form of displacements. The

DDD is commonly used to model the degradation of the solar cell parameters following irradiation with protons and electrons.[1]

An important physical parameter for the NIEL determination is the threshold energy for displacement E_{d_0}, which corresponds to the minimum energy required for a recoil atom to displace a Ga or As atom from its lattice position. This value has been measured via x-ray diffraction[2] and estimated via molecular dynamics simulations[3] to be in the range $E_{d_0} = 9-13$ eV.

In irradiated p-type GaAs solar cells following a standardized annealing regime at 333 K,[4] the remaining factors (RFs) for the short-circuit current density J_{SC} can be fitted with the classical equation $RF(J_{SC}) = 1 - C_x \log(1 + DDD/D_x)$ for all electron energies in the range of interest if an adapted threshold energy of

$E_d = 21$ eV is used in the NIEL calculation, as shown in Fig. 1(a). By using the same E_d value for the proton NIEL, the proton data collapse on the same degradation curve, which is then a pure function of the DDD only. The physical reason for the discrepancy between E_d and E_{d_0} was attributed[5] to the annealing of defects formed by recoils with energy lower than 21 eV. The degradation behavior of the open-circuit voltage V_{OC} and the recombination current density J_{02}, however, differ significantly from the J_{SC} trend, showing that not all the solar cell parameters degrade the same way. In particular, two features are observed in GaAs cells: (1) the proton DDD is more effective than the electron DDD in damaging V_{OC} and J_{02}, as visible in Figs. 1(b) and (c) and (2) the adapted value $E_d = 21$ eV leads to a good fit of the V_{OC} electron data only in the low–medium dose range and to a poor fit of the J_{02} electron data for all fluence values. For the latter parameter, a higher $E_d = 35$ eV would result in a better fit of the high-energy electron spectrum above 1 MeV, as shown in Fig. 1(d). With this E_d value, however, the NIEL of 0.5 MeV electrons would be virtually zero, in contradiction with the slight J_{02} degradation observed for this electron energy, as visible in Fig. 1(c).

Nevertheless, the adapted value $E_d = 21$ eV is generally used in the radiation analysis of GaAs-based solar cells. In the V_{OC} and J_{02} cases, empirical correction factors are defined as the ratio of the electron DDD (D_e) over the proton DDD (D_p) for a similar degradation level of the parameter, i.e., $R_{ep} = D_e/D_p$. The R_{ep} factors allow D_e to be converted in D_p and vice versa. In p-type GaAs cells, it has been shown[1,6] that $R_{ep}^{V_{OC}} \approx 3$ and $R_{ep}^{J_{02}} \approx 9.5$.

A detailed knowledge of the defects produced by the displacement damage and their electrical effectiveness on the macroscopic cell parameters would allow the physical meaning behind the R_{ep} factors and the adapted E_d values adopted in the treatment of solar cell remaining factors to be understood. Defect characterization in representative space component cells has been performed with deep-level transient spectroscopy (DLTS) on *ad hoc* mesa diode structures.[7] A similar characterization of different solar cell technologies has been performed by several authors[8,9] by means of non-transient capacitance methods. In this work, admittance spectroscopy proved to be a suitable tool for defect characterization in standardized 2×2 cm^2 GaAs component cells irradiated with protons and electrons at different energies and fluences. The nature and electrical characteristics of four defects are probed in the p-type GaAs base, allowing their damaging effectiveness in terms of solar cell J_{SC}, V_{OC}, and J_{02} to be estimated. The combined admittance-NIEL analysis suggests physical explanations for the values of E_d and the R_{ep} adopted in the DDD treatment of GaAs-based solar cell degradation data.

The paper is organized as follows: in Sec. II, the technology of the samples under test is presented, as well as the details of the relevant irradiation experiments and measurement setups; in Secs. III, IV, and V, the fitting routine of the solar cell admittance and the defect introduction rates is outlined in detail; in Sec. VI, the electrical characteristics of the irradiation-induced defect are presented, and the conclusions are drawn in Sec. VII.

II. EXPERIMENTAL DETAILS

The samples analyzed were 2×2 cm^2 bare GaAs n$^+$/ p component cells, fully representative of the middle sub-cell in lattice
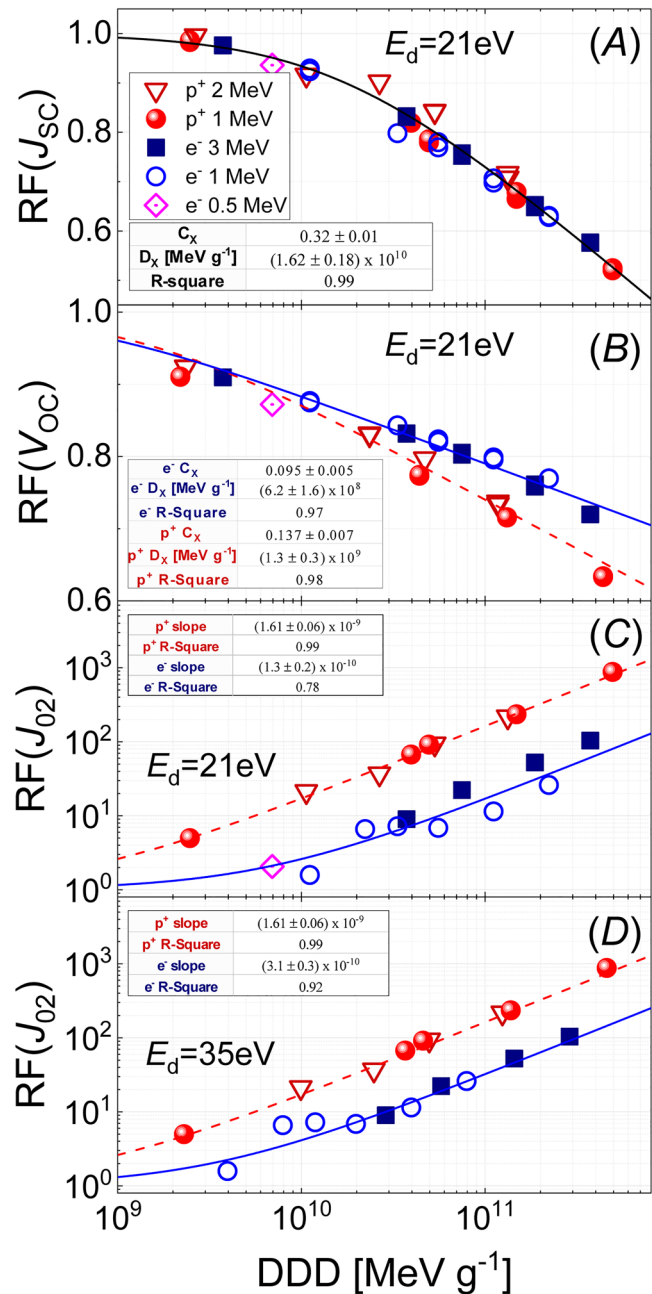

FIG. 1. GaAs component cell remaining factors of (a) short-circuit current density J_{SC}, (b) open-circuit voltage V_{OC}, and (c) recombination current density (J_{02}), with the DDD computed by using a threshold energy of $E_d = 21$ eV. (d) J_{02} remaining factor with an adapted $E_d = 35$ eV. Further details on the cells can be found in Sec. II.

matched, 30% efficient, triple junction $Ga_{0.5}In_{0.5}P/GaAs/Ge$ solar cells. The base layer was doped with a nominal acceptor concentration $N_a = 4 \times 10^{16}$ cm^{-3}, whereas the emitter layer had a donor concentration of $N_d = 10^{18}$ cm^{-3}. The cells featured surface field

layers at the back (BSF) and at the front (FSF) side, which were realized with higher bandgap material. All relevant material parameters for GaAs were taken from literature data.[10]

The solar cells were homogeneously irradiated at 300 K with 0.5, 1, and 3 MeV electrons and 1 and 2 MeV protons at different fluences Φ. The irradiation history of all samples is summarized in Table I. Following irradiation, the solar cells were annealed in three steps: (1) 48 h under AM0 condition at $T = 300$ K; (2) 24 h in dark conditions at $T = 333$ K, and (3) 24 h in dark conditions at $T = 370$ K. Annealing steps (1) and (2) were performed in accordance with the relevant ECSS space standards,[4] whereas step (3) was performed to ensure stable conditions during the admittance measurements that were carried out up to this temperature.

The admittance of the solar cells was measured with an E4980a precision LCR meter in dark conditions, in the temperature range 190 K < T < 370 K with steps of 10 K. The admittance was measured with a 0 V bias and an ac signal δv with a root-mean-square (rms) value ranging from 10 to 30 mV$_{\text{rms}}$, in the frequency range 20 Hz < f < 500 kHz. According to the Kramers–Kronig relations, only the capacitance data were used in the analysis. The accuracy of the capacitance measurements was better than 20 pF. The solar cell J_{SC}, V_{OC}, and J_{02} data for these cells have already been measured and published in the previous work.[6]

III. ADMITTANCE MODEL

The contribution of a discrete hole trap with homogeneous concentration N_{t} to the space-charge region (SCR) capacitance C_{SCR} under the stimulus of an external alternate bias $\delta v = v_{\text{ac}} \exp(2\pi f t)$ with amplitude v_{ac} and frequency f is modeled using the analytical approach proposed by Blood and Orton.[11] A deep level located at E_{t}

TABLE I. Irradiation history of GaAs component cells at $T = 300$ K.

Particle	Energy (MeV)	Fluence (cm^{-2})	Facility	No. of samples
e^-	0.5	1.4×10^{16}	TU Delft	2
e^-	1	1×10^{15}	TU Delft	1
e^-	1	2×10^{15}	Ecole Polytechnique	1
e^-	1	3×10^{15}	Ecole Polytechnique	1
e^-	1	5×10^{15}	TU Delft	2
e^-	1	1×10^{16}	TU Delft	2
e^-	1	2×10^{16}	TU Delft	2
e^-	3	2×10^{15}	TU Delft	2
e^-	3	5×10^{15}	TU Delft	2
e^-	3	1×10^{16}	TU Delft	2
p^+	1	8×10^{11}	CSNSM Orsay	1
p^+	1	1×10^{12}	CSNSM Orsay	1
p^+	1	3×10^{12}	CSNSM Orsay	2
p^+	1	1×10^{13}	CSNSM Orsay	2
p^+	2	4×10^{11}	CSNSM Orsay	1
p^+	2	2×10^{12}	CSNSM Orsay	1
p^+	2	5×10^{12}	CSNSM Orsay	2

above the valence band E_{V} is exposed to a hole flux $p \times v_{\text{th}}$, which is dependent on the position of the Fermi level E_{F}. Assuming an unitary degeneracy factor for the trap and negligible barrier lowering due to the Poole–Frenkel effect, the hole capture rate c_{p} and the emission rate e_{p} per unoccupied state are governed by the following relationships in thermal equilibrium:

$$c_{\text{p}} = \sigma_{\text{p}} v_{\text{th}} p = \sigma_{\text{p}} v_{\text{th}} N_{\text{V}} \exp\left(-\frac{E_{\text{F}} - E_{\text{V}}}{kT}\right),$$

$$e_{\text{p}} = c_{\text{p}} \exp\left(\frac{E_{\text{F}} - E_{\text{t}}}{kT}\right) = \sigma_{\text{p}} v_{\text{th}} N_{\text{V}} \exp\left(-\frac{E_{\text{t}} - E_{\text{V}}}{kT}\right), \quad (1)$$

where v_{th} is the rms velocity of holes in the valence band, N_{V} is the density of states in the valence band, and σ_{p} denotes the hole capture cross section. In the first half of the δv positive cycle, the modulation δE_{F} in the SCR leads to a trap-filling process with rate c_{p} and a modulation of the defect charge state per unit area δq_{t}. In the second half of the positive cycle, the filled traps are emptied by hole emissions with rate e_{p}. The same applies to the negative ac cycle. If δq_{a} denotes the charge variation due to the ionized acceptors N_{a} at the edge of the SCR, the current oscillation per unit area in response to the applied ac bias is $\delta i = \text{d}(\delta q_{\text{a}} + \delta q_{\text{t}})/\text{d}t$.

The charge modulation δq_{t} responds directly to the driving bias δv, provided that $f \ll e_{\text{p}}/\pi$. In this low-frequency range, the trap is activated and the charge contribution to the overall capacitance is due to both N_{a} and N_{t}: $C = C_{\text{SCR}} + \Delta C$. By making use of Poisson's equation in the SCR, the capacitance contribution ΔC associated with the deep level is evaluated as

$$\frac{\Delta C}{C_{\text{SCR}}} = \frac{N_{\text{t}}}{N_{\text{a}}}\left(\frac{1 - \frac{x_{\text{t}}}{W_{\text{SCR}}}}{1 + \frac{N_{\text{t}} x_{\text{t}}}{N_{\text{a}} W_{\text{SCR}}}}\right), \quad (2)$$

where W_{SCR} is the SCR width and x_{t} is the position in the SCR where $E_{\text{t}} = E_{\text{F}}$. For $N_{\text{t}} \ll N_{\text{a}}$, Eq. (2) can be further simplified to

$$\frac{\Delta C}{C_{\text{SCR}}} = \frac{N_{\text{t}}}{N_{\text{a}}}\sqrt{\frac{E_{\text{t}} - E_{\text{F}_{\text{p}}}}{q\,V_{\text{bi}}}}, \quad (3)$$

where V_{bi} is the built-in voltage and $E_{\text{F}_{\text{p}}}$ is the Fermi level in the p-side neutral region. At higher frequencies, the trap cannot emit holes during the emitting cycle since $f \gg e_{\text{p}}/\pi$, therefore $\delta q_{\text{t}} = 0$ and $C = C_{\text{SCR}}$ due solely to N_{a}.

A frequency-dependent expression for the total capacitance per unit area is obtained[11] from the complex part of $(2\pi f)^{-1}\delta i/\delta v$,

$$C(f) = C_{\text{SCR}} + \frac{\Delta C}{1 + (f/f_{\text{t}})^2}. \quad (4)$$

Its derivation considers the change in majority carrier concentration in the SCR based on the combined response of the shallow acceptors as well as the trap to the applied bias. The occupation probability of the trap is calculated with the help of the capture and emission rates according to Eq. (1). The characteristic frequency f_{t} defines the transition between the two states of the trap behavior

and is derived as

$$f_t = \frac{e_p}{\pi}\left(1 + \frac{x_t N_t}{W_{SCR} N_a}\right). \tag{5}$$

The term in the brackets of Eq. (5) expresses the coupling between the response of the deep level and the shallow acceptors. For $N_t \ll N_a$, it can be neglected and the transition frequency is given in Eq. (1). If the temperature dependence of f_t is known, an Arrhenius fit allows the trap energy level E_t to be extracted, as well as the subsequent capture cross section σ_p, considering that the product $N_V v_{th}$ has a T^2 temperature dependence, whereas σ_p is assumed to be temperature independent.

The C–f characteristic exhibits a step-like behavior centered at $f = f_t(T)$ according to Eq. (4). At any given temperature, f_t is the frequency point with maximum derivative and is easily identified in a measured spectrum as the peak of the functional $-f\,dC/df$. The depletion capacitance C_{SCR} is the value measured when ideally no deep-level contributes and no carrier freeze-out occurs, i.e., $f \gg \max[e_p]$ and $f \ll \tau_\epsilon^{-1}$, with τ_ϵ denoting the dielectric relaxation time of the dopant atoms in GaAs.

In the real case of n deep levels characterized by a continuous distribution of available states in the bandgap centered around the energy value E_{t_0}, the term N_t in Eq. (3) is replaced by the total density of states $N_T(E)$. For each defect level, a Gaussian-shaped distribution is considered, characterized by a density function,

$$N_{T,n}(E) = \frac{N_{t_0,n}}{\lambda_n \sqrt{2\pi}} \exp\left[-\frac{1}{2}\left(\frac{E - E_{t_0,n}}{\lambda_n}\right)^2\right], \tag{6}$$

where N_{t_0} is the total integrated concentration and λ is the distribution width defining the localization of the electrons in the level. By replacing N_t with $N_T(E)$ and E_t with the variable E in the previous equations, the admittance formalism presented so far is extended to the case of Gaussian distributions of states in the bandgap. The total capacitance is thus obtained by substituting Eqs. (3) and (5) in Eq. (4) and integrating over the energy E in the bandgap. If all energy levels are not used in absolute terms but are referenced to the valence band according to $E' = E - E_V$, the following expression is derived:

$$C = C_{SCR} + \sum_{k=1}^{n} \frac{C_{SCR}}{\lambda_k \sqrt{2\pi q\, V_{bi}}} \frac{N_{t_0,k}}{N_a}$$

$$\times \int_{E'_{F_p}}^{E'_{F_p} + qV_{bi}} \frac{\sqrt{E' - E'_{F_p}}\, \exp\left[-\frac{1}{2}\left(\frac{E' - E'_{t_0,k}}{\lambda_k}\right)^2\right]}{1 + \left\{\frac{\pi f \exp[E'/(kT)]}{\sigma_{p,k} v_{th} N_V}\right\}^2} dE'. \tag{7}$$

The value E'_{F_p} is obtained as $E'_{F_p} = E'_i - kT\, ln(N_a/n_i)$, where E'_i and n_i are the intrinsic Fermi level position and the intrinsic carrier concentration, respectively. Deep levels outside the integral boundaries in Eq. (7) do not cross E_F in the p-side SCR and thus cannot contribute to the capacitance.

IV. FITTING PROCESS

A. General considerations

A representative C–f–T spectrum for irradiated GaAs solar cell is illustrated in Fig. 2. Two main capacitance steps CS_1 and CS_2 are visible in the blue and orange area of the plot, respectively. On the f–T plane, the projection of the function $-f\,dC/df$ facilitates to pinpoint the f_t–T tracks. The evolution of CS_1 and CS_2 with temperature occurs separately in different areas of the f_t–T plot without a significant overlap: CS_1 in the range $LT = \{190\,K < T < 260\,K\}$ and CS_2 in the range $HT = \{290\,K < T < 370\,K\}$. The drop-off at high frequencies is caused by the resonance of the total cell capacitance with the stray inductance of the external circuit. At low temperatures, the hole conduction at the BSF hetero-interface[12] results in a big capacitance drop. It limits the accessible frequency range and masks the effect of potential shallower levels below 190 K.

The fitting of the C–f–T surface with Eq. (7) requires the knowledge of the exact value of $C_{SCR}(T)$ from which in turn $N_a(T)$ and later N_{t_0} can be accurately determined. Theoretically, C_{SCR} could be easily extracted for every temperature as the capacitance value measured in the high-frequency range, although this—as mentioned before—has limited accessibility. Therefore, C_{SCR} should be included as a fitting parameter in Eq. (7). In addition, C_{SCR} is temperature-dependent due to the varying degree of ionization of the dopant atoms on both n- and p-type sides of the junction. The temperature dependence is not a linear function over the wide temperature range investigated,[13] thus leading potentially to an ambiguous fit. However, its value can be linearized separately in the temperature range LT and HT by using the expression $C_{SCR}(T) = \alpha T + \beta$, with constants α and β for each temperature regime.
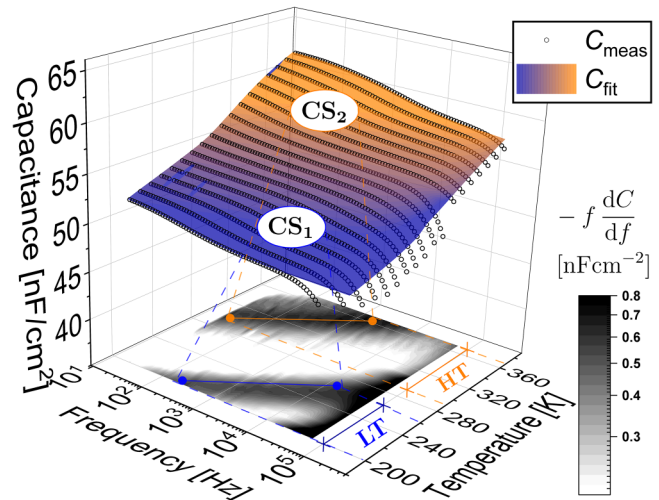

FIG. 2. C–f–T spectra of p-type GaAs component cell irradiated with 3 MeV electron at a fluence of $5 \times 10^{15}\,cm^{-2}$. Measured data points are represented by open circles, whereas the surface fit is obtained using Eq. (7). The surface color map distinguishes two distinct capacitance steps CS_1 (blue area) and CS_2 (orange area). On the f–T plane, the projection of the function $-f\,dC/df$ is illustrated.

The fitting process is thus split into two separate routines for the LT and the HT regimes, leading to the determination of two separate values of $C_{SCR}^{LT}(T)$ and $C_{SCR}^{HT}(T)$ and avoiding ambiguities arising from single-temperature capacitance data. The splitting of the fitting process allows further simplification in the single routines. The defect responsible for the CS_1 step in the LT regime is always activated in the HT regime, i.e., the f_t associated with CS_1 shifts out of the measurable frequency range in the HT regime according to Eqs. (1) and (5). For this reason, the concentration of the defect responsible for CS_1 can be lumped together with N_a in the value of C_{SCR}^{HT}. This approach is in line with the treatment of all the defects independently from one another and requires less computational resources. By embracing this approach, it should be noted that the resulting C_{SCR}^{HT} includes the contribution of the CS_1 defect concentration and N_a, whereas C_{SCR}^{LT} is only due to N_a. In summary, the splitting of the fitting routine in the LT and HT range allows the temperature dependency of C_{SCR} to be linearized in the two regimes, thus leading to an unambiguous fit. Moreover, it improves the computational efficiency by reducing the number of defects required in Eq. (7) per each fitting routine.

B. Parameter fitting

The number of defects n included in each fitting routine is determined by the number of distinguishable peaks f_t found in the functional $-f\,dC/df$: one single defect—labeled H1—in the LT range, and three defects—labeled H2, H3, and H4—in the HT range. The three defects in the HT range are not distinguishable in Fig. 2 because of the limitation in the resolution of the plot. The parameters to be determined are E'_{t_0}, N_{t_0}, σ_p, and λ for each defect,

as well as the coefficients α and β that determine $C_{SCR}^{LT,RT}(T)$ for the two temperature regimes. The fitting of the C–f–T surface is performed in three steps,

(i) The trap signature $f_t(T)$ is fitted with the Arrhenius equations (5) and (1), yielding E'_{t_0} and an initial value of σ_p.
(ii) The initial values for α, β, N_{t_0}, and λ are chosen manually according to their respective influences on the C–f curves.
(iii) The refined values for σ_p, N_{t_0}, and λ, as well as the coefficients α and β are obtained with the help of the algorithm that minimize the residual function S_{rms},

$$S_{rms} = \sqrt{N_{point}^{-1} \sum_T \sum_f (C_{meas} - C_{fit})^2}, \qquad (8)$$

where N_{point} is the number of useful data points.

The results of the fitting process for all cells, particle energies, and fluences are summarized in Table II. For E'_{t_0}, the uncertainty range of the Arrhenius fit is indicated. The uncertainty associated with the remaining fitting parameters is obtained with a Monte Carlo approach[14] and represents the 95% confidence interval obtained over a set of 100 routines, where the starting values for each parameter are varied randomly in a range of two orders of magnitude with respect to the expected value. It is useful for the manual determination of the starting parameters in step (ii) to consider the contribution of each fitting parameter in the step-like shape of the C–f curve: $C_{SCR}^{LT,HT}$ is the baseline capacitance signal, which is easily accessible in the high-frequency range on the lower temperature curves for each regime. The linearization of $C_{SCR}^{LT,HT}(T)$

TABLE II. Defect parameters resulting from the fitting routine of the GaAs component cells. The first column indicates the irradiation particle, energy (in MeV), and fluence (in cm^{-2}).

| | H1 | | | H2 | | | H3 | | | H4 | | |
| | $E'_{t0} = (0.29 \pm 0.01)$ eV | | | $E'_{t0} = (0.61 \pm 0.02)$ eV | | | $E'_{t0} = (0.68 \pm 0.03)$ eV | | | 0.45 eV $< E'_{t0} <$ 0.55 eV | | |
Cell	N_{t0} (cm^{-3}) $\times10^{14}$	σ_P (cm^{-2}) $\times10^{-16}$	λ (eV) $\times10^{-3}$	N_{t0} (cm^{-3}) $\times10^{14}$	σ_P (cm^{-2}) $\times10^{-16}$	λ (eV) $\times10^{-3}$	N_{t0} (cm^{-3}) $\times10^{14}$	σ_P (cm^{-2}) $\times10^{-16}$	λ (eV) $\times10^{-3}$	N_{t0} (cm^{-3}) $\times10^{14}$	σ_P (cm^{-2}) $\times10^{-16}$	λ (eV) $\times10^{-3}$
e0.5 1.4×10^{16}	0.8 ± 0.3	2 ± 1.4	20 ± 9	…	…	…	…	…	…	…	…	…
e1 1×10^{15}	1.5 ± 0.6	4.7 ± 3.4	33 ± 15	…	…	…	…	…	…	…	…	…
e3 3×10^{15}	5.8 ± 1.6	3.4 ± 2.5	14 ± 7.4	0.6 ± 0.4	40 ± 28	19 ± 19	2.5 ± 0.7	20 ± 30	36 ± 38	0.5 ± 0.3	40	78 ± 61
e5 5×10^{15}	9.1 ± 1.6	4.5 ± 2.5	25 ± 7	0.9 ± 0.5	109 ± 80	10 ± 10	3.9 ± 0.6	80 ± 60	46 ± 24	0.7 ± 0.2	109	33 ± 17
e1 1×10^{16}	16 ± 3	3.7 ± 1.6	18 ± 3	1.7 ± 0.3	104 ± 44	11 ± 3	6.9 ± 1.2	83 ± 35	35 ± 6	1.8 ± 0.4	104	50 ± 10
e1 2×10^{16}	33 ± 6	3.5 ± 1.4	17 ± 3	4.8 ± 0.8	82 ± 45	12 ± 4	11 ± 2	77 ± 42	26 ± 5	3 ± 0.5	82	49 ± 8
e3 2×10^{15}	10 ± 3	4 ± 1.7	34 ± 6	4 ± 0.5	67 ± 28	29 ± 5	2.8 ± 0.6	45 ± 19	26 ± 4	2 ± 0.2	67	40 ± 10
e3 5×10^{15}	25 ± 3	4.7 ± 1.5	32 ± 5	12 ± 1.4	72 ± 30	36 ± 5	5.7 ± 0.7	57 ± 24	31 ± 5	6 ± 0.7	72	40 ± 3
e3 1×10^{16}	58 ± 5	3.4 ± 0.9	14 ± 4	28 ± 3.3	76 ± 16	35 ± 3	10 ± 1.3	57 ± 12	31 ± 3	10 ± 1.2	76	40 ± 4
p1 8×10^{11}	3.6 ± 1.3	4.9 ± 3.6	45 ± 8	…	…	…	…	…	…	…	…	…
p1 1×10^{12}	4.6 ± 1.3	4.9 ± 3.6	41 ± 8	3 ± 0.8	191 ± 111	44 ± 6	1.5 ± 0.4	54 ± 39	47 ± 6	2.5 ± 0.7	191	50 ± 6
p1 3×10^{12}	9.5 ± 2	3.9 ± 1.6	26 ± 8	12 ± 2.3	221 ± 93	49 ± 7	3.3 ± 0.6	50 ± 21	46 ± 6	7 ± 1.3	221	40 ± 5
p1 1×10^{13}	34 ± 3.6	3.2 ± 1	39 ± 8	45 ± 2.2	224 ± 51	65 ± 8	5.4 ± 0.6	25 ± 21	35 ± 6	16 ± 0.7	224	30 ± 4
p2 2×10^{12}	…	…	…	3.5 ± 0.7	138 ± 51	70 ± 10	0.2 ± 0.2	125 ± 55	26 ± 4	1.9 ± 0.3	138	84 ± 25
p1 5×10^{12}	10 ± 6.9	4 ± 2.5	61 ± 8	9.7 ± 0.3	147 ± 68	71 ± 10	0.6 ± 0.5	14 ± 10	36 ± 20	4 ± 1.3	147	40 ± 25

ensures coherent values also at the temperatures where the high-frequency capacitance is not accessible due to the aforementioned limitations. The steepness of the capacitance step is solely determined by the parameter λ in Eq. (7). The amplitude of the capacitance step is thus mainly determined by the parameter N_{t_0}. The f_t position is determined by E_{t_0} and σ_P according to Eq. (5) with $N_{t_0} \ll N_a$. If E_{t_0} is fixed by the Arrhenius fit, the position of f_t is solely determined by σ_P. It should be mentioned that, as E_{t_0} is fixed for all the irradiated cells, a slight variation within the uncertainty of the energy level is compensated by a large variation of σ_P according to Eq. (1), thus explaining the high uncertainty of this parameter.

Taking into account the accuracy of the LCR meter and the uncertainty of the doping levels of the cells, a value of $N_{t_0} \approx 8 \times 10^{13}$ cm^{-2} represents the minimum concentration sensitivity, resulting in a detection factor $N_{t_0}/N_a \approx 2 \times 10^{-3}$. It has to be noted that CS$_1$ and CS$_2$, ascribed to the effect of irradiation-induced defects, have been checked against other possible causes, e.g., resistance effects, dielectric relaxation, and hetero-interface barriers.

The effect of all defects on the cell capacitance is distributed over the entire f–T domain. It is possible to produce a single plot, which condenses all data of the two f–T domains in a unique

FIG. 3. (a) Scaled admittance signal $-f\mathrm{d}C/\mathrm{d}f$ and (b) combined density of states in the bandgap of p-type GaAs component cells irradiated with a similar amount of DDD introduced by 1 and 3 MeV electrons and 1 MeV protons.

curve so that the effect of all the defects is visible at a glance. This can be achieved by plotting $-f\mathrm{d}C/\mathrm{d}f$ over a scaled frequency axis computed as $fT^2 f_o \exp(E_f/kT)$, where f_o is a constant and the value E_f is an exponential scaling factor, which equals the activation energy of H2 for the spectra in the HT temperature range and of H1 in the LT temperature range. The resulting plot is illustrated in Fig. 3(a), and the single contributions of H2, H3, and H4 in the HT range can be differentiated in the low scaled-frequency range. In addition, the density of states in the GaAs bandgap extracted from the fitting process is depicted in Fig. 3(b).

V. NIEL DEFECT ANALYSIS

A. NIEL calculation

The defect concentration data obtained from the admittance fitting routine are correlated with the displacements created by the primary particle of energy ξ in the crystal through all recoils. Under the assumption that the particle slow-down within the layers is negligible, the DDD is calculated as

$$\mathrm{DDD} = \int_\xi \mathrm{NIEL}(\xi)\phi(\xi)\,\mathrm{d}\xi. \tag{9}$$

The particle NIEL in the GaAs compound is estimated by assuming a linear combination of the NIEL of the individual elements, weighted according to their atomic weight (Bragg's rule). For the single element, the NIEL is computed analytically as

$$\mathrm{NIEL}(\xi) = \frac{N}{A} \int_{E_d}^{E_{max}} E_R L(E_R) \frac{\partial \sigma_{Cs}(\xi, E_R)}{\partial E_R}\,\mathrm{d}E_R, \tag{10}$$

where N is the Avogadro number and A is the atomic mass. The integration variable E_R is the recoil energy. E_d is the minimum energy transferred to a recoil that results in Ga and As displacements. In Secs. V B–VIII, the NIEL and related DDD are marked with the subscript "0" when the value $E_d = E_{d_0} = 10$ eV is adopted. E_{max} is the maximum energy that the particle can transfer to the recoil. $\partial \sigma_{Cs}/\partial E_R$ is the differential cross section for Coulomb scattering, quantifying the probability that the primary particle of energy ξ generates a recoil with energy E_R. $L(E_R)$ is the recoil partition function, which quantifies the fraction of E_R that goes into displacements. It is computed by means of the Robinson formulation[15] of the Lindhard partition function.[16] For the electron $\partial \sigma_{Cs}/\partial E_R$, the Mott differential cross section[17] with the approximation proposed by Boschini et al. is adopted,[18] accounting for screened Coulomb fields, finite size, and rest mass of the target nuclei. For protons, the Wentzel–Molière expression[19] is used. The resulting NIEL values are similar to the one calculated via the online SR-NIEL calculator.[20] The NIEL$_0$ contribution factor $\chi(E)$, defined as

$$\chi(E) = \frac{\int_{E_{d_0}}^{E} E_R\, L\, \frac{\partial \sigma_{Cs}}{\partial E_R}\,\mathrm{d}E_R}{\int_{E_{d_0}}^{E_{max}} E_R\, L\, \frac{\partial \sigma_{Cs}}{\partial E_R}\,\mathrm{d}E_R}, \tag{11}$$

quantifies the NIEL$_0$ contribution of the recoil spectrum from E_{d_0} up to the energy E. From the plots of the $\chi(E)$ factor, reported as a
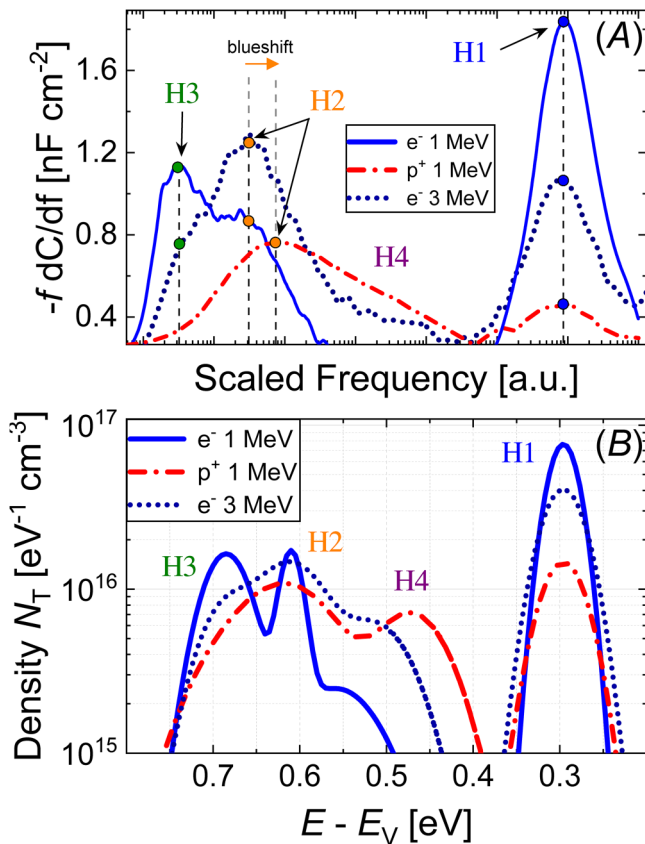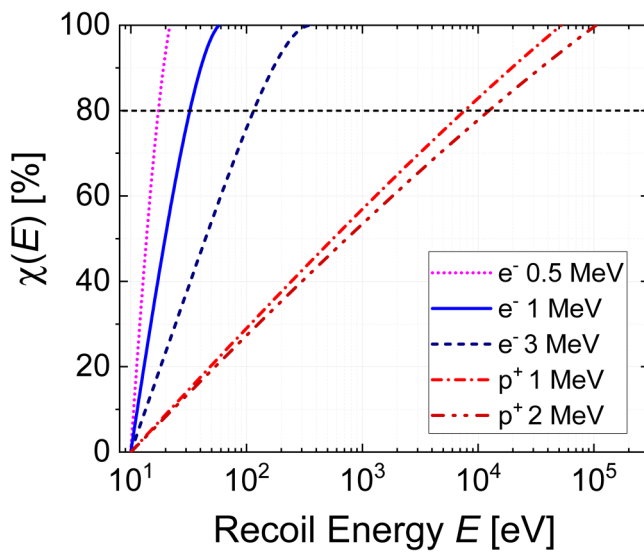
FIG. 4. Relative NIEL contribution $\chi(E)$ originating from recoils with energies below E for 0.5, 1, and 3 MeV electrons and 1 and 2 MeV protons in GaAs.

percentage in Fig. 4, it is possible to identify the effective recoil spectrum that deposits the DDD for each irradiating particle. For instance, 80% of the damage caused by 1 MeV electrons is due to recoils with energy below 40 eV. The same recoil spectrum accounts for only 40% of the damage in the 3 MeV electron case and for only 10% of the damage in the 1 MeV proton case. The recoil spectrum triggered by the irradiating particle has several implications on the formation of the defects within the lattice. Recoils with energy just above E_{d_0} can only create one or no additional displacement. Therefore, the displacements produced by 1 MeV electrons, which can trigger recoils up to few tens of eV, are generated in a region of the lattice not populated by many other neighboring point defects. The displaced atoms are most likely isolated—i.e., they do not interact with other closely spaced lattice imperfection. In the proton case, on the other hand, recoils with much higher energy have a large contribution to the $NIEL_0$. A high-energy recoil can trigger a long-range displacement cascade resulting in the formation of highly damaged regions,[21] where closely spaced point defects interact and form stable clusters. The size of these clusters can extend up to several GaAs lattice constants.[22]

B. Fitting of the defect E_d

The admittance measurements yield individual defect concentrations as a function of different particle energies and fluences. Therefore, it is a straightforward approach to see whether they can be collapsed onto a single characteristic N_{t_0}–DDD curve. It will be shown in Sec. VI that the data fall onto a single straight line if an adapted E_d in the electron case is used. The value E_d can be directly related to the physical defect configuration. It represents the minimum recoil energy whose displacements contribute effectively to the final defect structure. When E_d approaches the threshold energy for Ga and As displacement E_{d_0}, the defect unit cell is made

up of a single-displacement structure, i.e., a simple Frenkel pair. When $E_d > E_{d_0}$, on the other hand, the defect unit cell is composed of a more complex structure, such as defects with higher formation energy (e.g., antisites) or multi-displacement defects (e.g., divacancies). The fitting of E_d for a given defect such that the defect introduction rates fall on the same NIEL curve for all electron energies is therefore a way to draw conclusions on the physical defect configuration in the lattice directly from admittance measurements. Only the electron data are used for this procedure due to the higher sensitivity of the electron NIEL to E_d compared to the proton NIEL in the energy range of interest. It has to be noted that the NIEL is based on a purely analytical calculation. The adapted threshold energy for the defect in question is a way to achieve the correct energy scaling with regard to the introduction rate of different particles. No conclusion on relative contributions of other defects in the displacement damage can be drawn from this fitting alone.

The electron displacement introduction rate (eDIR) is defined as $eDIR = N_{t_0}/D_e$ in analogy to the defect introduction rate $k_t = N_{t_0}/\Phi$. Likewise, pDIR is defined with respect to the adapted proton dose. When eDIR and pDIR are different, the different particle effectiveness is accounted for by the factor $R_{ep}^d = pDIR/eDIR$, defined in analogy to the electrical R_{ep}. The defect R_{ep}^d allows D_e to be scaled so that the N_{t_0}–D_e plot falls onto the N_{t_0}–D_p plot.

While a similar approach has also been followed in the past for the solar cell macroscopic electric parameters, any conclusions, in this case, were hampered by the fact that only the combined behavior of all defects, weighted by their electrical effectiveness, could be studied. Finally, it has to be noted that since the cells were irradiated at 300 K and all measurements were performed after 370 K annealing, an annealed defect configuration was probed in all cases.

VI. IRRADIATION-INDUCED DEFECTS

A. H1

The capacitance step CS_1 is characterized by a clear, distinguishable, single peak in the $-f\,dC/df$ functional, thus allowing an easy determination of $f_t(T)$. By making use of Eq. (5), the energy level associated with the defect, labeled H1, is found: $E'_{t_0} = 0.29\,\text{eV}$. The fitting of H1 introduction rates with the electron NIEL yields $E_d = 21\,\text{eV}$, which suggests that the defect is either formed by isolated antisites[23] or a different double-displacement defect. A similar energy level in irradiated p-type GaAs has already been reported in the literature.[24,25] The N_{t_0}–DDD and the introduction rate plots are reported in Figs. 5(a) and 5(b). In Fig. 5(b), the NIELs computed with different E_d values are superimposed in order to illustrate the sensitivity of the E_d fitting process.

eDIR and pDIR coefficients of 1.4×10^4 and $7.1 \times 10^3\,\text{g cm}^{-3}\,\text{MeV}^{-1}$ result, respectively, thus yielding $R_{ep}^d = 0.5$. The electron dose D_e is twice as effective as the corresponding proton D_p in producing H1.

B. H2 and H3

The capacitance step CS_2 for electron-irradiated cells is characterized by the presence of two overlapping peaks in the $-f\,dC/df$ functional, which are attributed to two separate irradiation-induced defects, H2 and H3. The contributions of H2 and H3 are
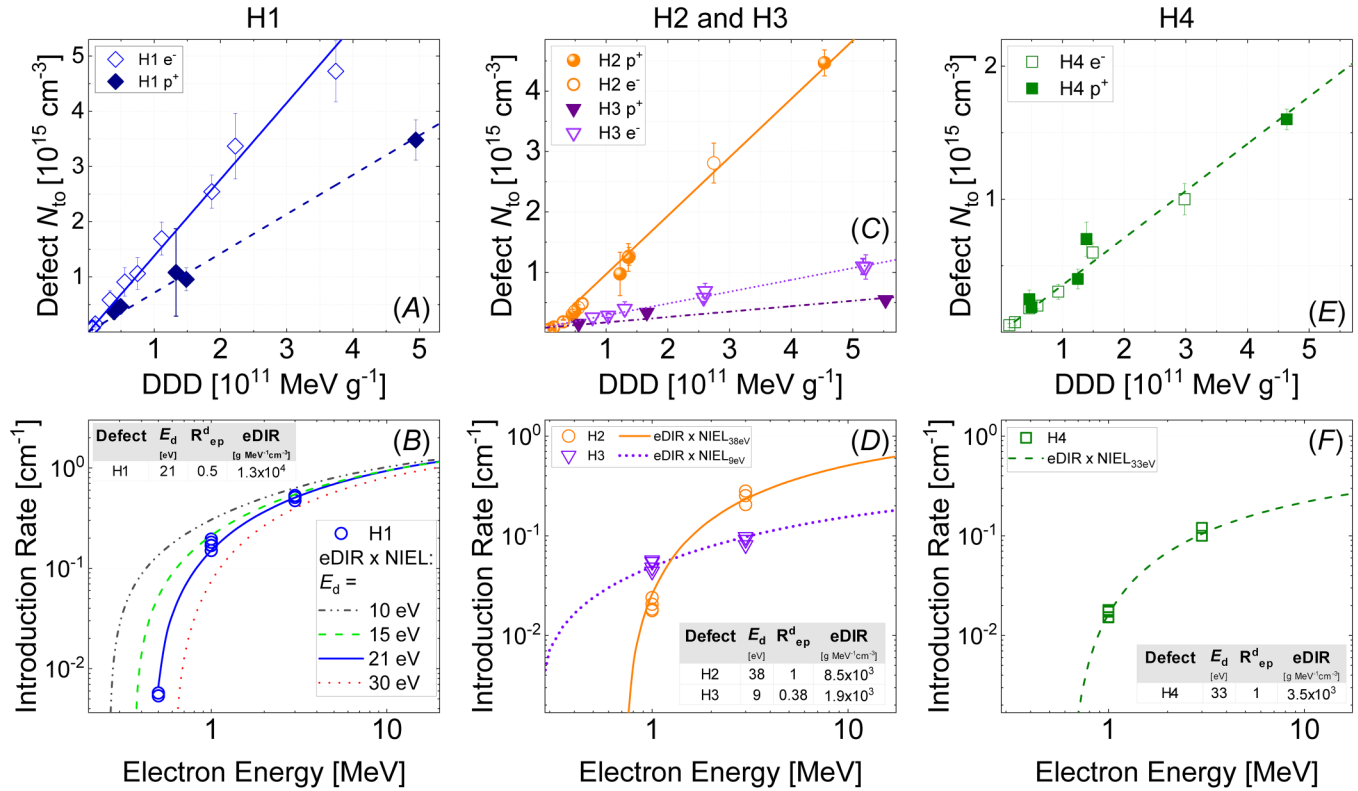
FIG. 5. Defect concentration as a function of adapted DDD and introduction rate as a function of particle energy for (a) and (b) H1, (c) and (d) H2 and H3, and (e) and (f) H4 in p-type GaAs component cells. The adapted DDD for each defect is computed by using the appropriate E_d values, reported in the insets in (b), (d), and (f).

de-coupled by performing a Gaussian de-convolution on the $-f\,dC/df$ data. In this way, the single $f_t(T)$ are extracted and fitted with Eq. (5), leading to two energy levels $E'_{t_0} = 0.61$ eV and $E'_{t_0} = 0.68$ eV for H2 and H3, respectively. In the proton case, on the other hand, the peak associated with H3 is only detectable in the higher fluence cases. The NIEL analysis of the electron data yields E_d values for H2 and H3 of 38 eV and 9 eV, respectively. The low E_d value for H3 suggests that it can be ascribed to a single-displacement defect, i.e., a Frenkel pair. On the other hand, H2 can be ascribed to a more complex defect structure. The energy level of H2 has been associated in the literature with the single donor configuration of the EL2 defect,[26,27] possibly due to As antisites (As_{Ga}) or more complex structures involving As_{Ga} coupled with an As interstitial.

The N_{t_0}–DDD plots are reported in Fig. 5(c), whereas the eDIR and R^d_{ep} factor are reported in Fig. 5(d). The defect H3 exhibits an $R^d_{ep} = 0.38$, whereas $R_{ep} = 1$ is found for H2. A begin-of-life H3 concentration of about $(9 \pm 2) \times 10^{13}$ cm^{-3} is obtained in the linear fit of both the N_{t_0}-D_e and N_{t_0}–D_p plots. This indicated that H3 may be present in the material already prior irradiation.

C. H4

A small shoulder characterizes the H2 peak, as visible in Fig. 3(a) for the proton and 3 MeV electron cases. This capacitance

contribution is attributed to the deep level H4. Since only a featureless peak is detected in the $-f\,dC/df$ plots, it is not possible to determine the trap $f_t(T)$. The H4 contribution is included in the admittance model by using a fixed value of σ_p as the one of H2. In this way, the fitting routine yields the apparent H4 energy level, which shows variations in the range $0.45\,eV < E^*_{t_0} < 0.55\,eV$ for the different samples analyzed. The NIEL analysis yields a value of $E_d = 33$ eV and $R^d_{ep} = 1$.

VII. DISCUSSION

A. Effective NIEL*

With the knowledge of the absolute number of defects generated and the associated defect energy E_d, the total displacement damage can be calculated for each irradiating particle type and energy. The actual NIEL introduced, denoted as NIEL*, can be computed by taking into account each single defect introduction rate with the associated threshold energy,

$$\text{NIEL}^* = \rho^{-1} \sum_{i=1}^{n} (k_t \times E_d)_i, \qquad (12)$$

where ρ is the material density and n is the total number of type of defects introduced into the material; in this case, $n = 4$. The results

for H1–H4 are reported in Fig. 6. The theoretical $NIEL_0$ curves, computed using $E_{d_0} = 10\,eV$, are also superimposed using solid lines. The measured $NIEL^*$ values deviate from the theoretical $NIEL_0$ by a factor of 10. The missing $NIEL^*$ contribution responsible for this gap is expected to arise from defects that cannot be gauged via admittance spectroscopy in p-type samples, i.e., electron traps, defects located below E_{F_p} or whose energy level does not lie in the forbidden bandgap. A complementary analysis of at least the electron traps located in the upper half of the bandgap is required to arrive to a complete estimation of the $NIEL^*$. By considering only the introduction rates of the electron traps E1–E5 detected in irradiated n-type GaAs cells (1 MeV e^- data from Pons and Bourgoin[28]), an approximated $NIEL^*$ close to $NIEL_0$ can be estimated. It has been demonstrated in the past that these traps are also introduced in p-type GaAs.[27] Therefore, assuming comparable introduction rates of E1–E5 for n- and p-type materials, the bulk of the gap between $NIEL^*$ and $NIEL_0$ is due to the missing contribution of E1–E5 in Eq. (12).

Furthermore, it should be mentioned that the $NIEL_0$ value accounts for the non-ionizing energy deposited by irradiating the material at 0 K. It has been already recognized that the theoretical NIEL is not necessarily proportional to the total number of defects formed after irradiation[21] because of non-linear processes taking place in the lattice, e.g., the formation of clustered regions and the defect annihilation during both the irradiation experiment and the post-annealing treatment.[29] Although a general conclusion cannot be drawn based solely on the data available from this analysis, it is remarkable how the $NIEL^*$ relative to H1–H4 falls on an attenuated $NIEL \times 10^{-1}$ curve computed with $E_d = 21\,eV$, as shown in Fig. 6. Despite the fact that the H1 defect with $E_d = 21\,eV$ is the most prevalent defect, this E_d value is thus not representative of any

particular defect structure, but rather an empirical value with which it is possible to describe the introduction of the effective $NIEL^*$ in p-type GaAs in the form of stable defects H1–H4. It follows that the reference NIEL calculated with $E_d = 21\,eV$ can be used to compare a similar level of damage in terms of H1–H4 defects for cells irradiated with different particles and energies. Since no cell electrical parameters were involved in this derivation, it can be further concluded that this threshold energy is a GaAs material-specific parameter, independent of the detailed electrical device design.

B. Relative defect introduction

Incident particles, depending on their mass and energy, can trigger a vastly different recoil spectrum, as shown in Fig. 4. An obvious question is whether this affects the relative introduction probability of different defects. To address this topic further, a DDD of $2 \times 10^{11}\,MeV\,g^{-1}$ is chosen. With the help of a NIEL with 21 eV threshold energy, the required fluence of 1 and 3 MeV electrons as well as 1 MeV protons is calculated and the associated number of defects introduced is extracted from Table II with the help of a linear fit. The use of a $E_d = 21\,eV$ is essential for this comparison since only this threshold energy correctly quantifies the relative contribution of the H1–H4 defects in the overall displacement damage, as discussed in Sec. VII A. The absolute and relative defect concentrations are reported in the pie charts in Fig. 7.

The recoil spectrum triggered by the particles has a significant role in defining the relative concentration of the individual defects. As the energetic content of the recoil spectrum increases, it is more likely that defects with high E_d—such as H2 and H4—are generated, and defects with lower E_d—such as H1 and H3—account for a smaller fraction of the total damage.

C. Macroscopic parameter degradation

Due to the different electronic parameters found in H1–H4, a different damaging effectiveness with respect to the solar cell macroscopic electrical parameters is expected. The ultimate cause of a solar cell electrical parameter degradation is the reduction of the carrier lifetime $\tau_{n,p}$ within the solar cell neutral (J_{SC}) and depleted regions (V_{OC} and J_{02}), which is related to the defect parameters by $\tau_{n,p}^{-1} \propto \sigma_{n,p} v_{th} N_{t_0}$. If the electronic structure of the defect does not depend on the type and energy of the irradiating particle, its capture properties $\sigma_{n,p}$ are well defined and identical in the different irradiated cells. As a result, the degradation due to this class of defects occurs due to an increase of N_{t_0} as more displacements occur within the semiconductor. The damaging effectiveness of each defect on the solar cell J_{SC}, J_{02}, and V_{OC} can thus be estimated by means of correlation coefficients r resulting from the Pearson analysis between the parameter remaining factors and the defect N_{t_0}. When r approaches $+1$ (-1), a significant positive (negative) correlation between the parameters is found. Pearson's r coefficients for H1–H4 defects are reported in the color map of Fig. 8. Moreover, the Pearson analysis is extended to the DDD computed with $E_d = 21\,eV$ (D_{21eV}), which is representative of the actual scaling of the relative abundance of the defects H1–H4 with particle energy, as discussed earlier.
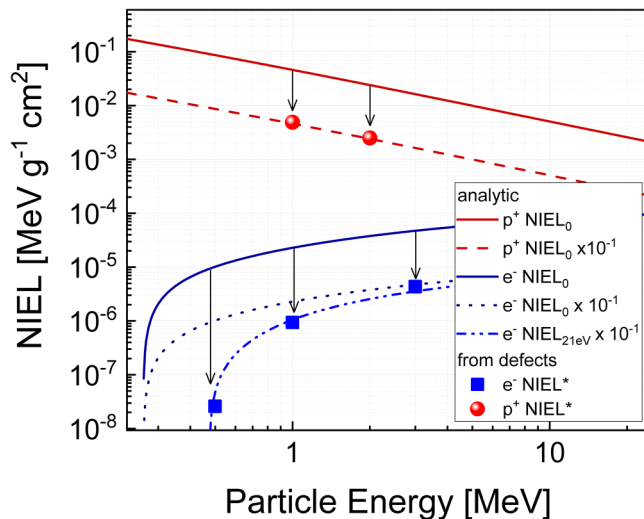

FIG. 6. Measured (data points) effective $NIEL^*$ in proton and electron-irradiated p-type GaAs computed with Eq. (11). The theoretical NIEL (solid curves) is calculated according to Eq. (10) with different threshold energies and superimposed to the plot.
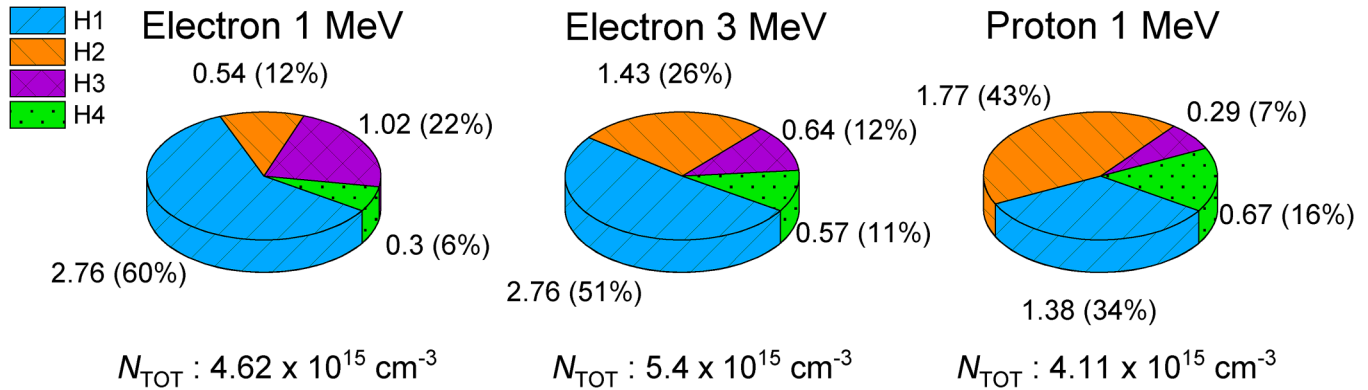
FIG. 7. Absolute (in units of 10^{15} cm^{-3}) and relative (N_{t_0}/N_{TOT}) defect concentration for the same amount of DDD $= 2 \times 10^{11}$ MeV g^{-1} introduced by 1 and 3 MeV electrons and 1 MeV protons in p-type GaAs component cells, computed with $E_d = 21$ eV. The total sum of the defects N_{TOT} is also reported for each case.

All defects exhibit a negative correlation with J_{SC} and, therefore, they are all damaging J_{SC} to a certain extent. The good correlation of the J_{SC} degradation with D_{21eV} ($r = -0.98$) indicates that it is likely that H1–H4 are the main defects responsible for the J_{SC} damage. These results are fully in line with the J_{SC} fit in Fig. 1. The total number of defects H1–H4 introduced by particles of different energies varies by a factor of 1.3 at most for the same amount of D_{21eV}, according to the findings shown in Fig. 7. Thus, the good correlation of J_{SC} with D_{21eV} can also be interpreted in terms of a good correlation to the sum of the defects. From this, it can be concluded that the minority carrier capture cross sections of H1–H4 are in a similar range and cannot differ by orders of magnitude.

On the other hand, V_{OC} and J_{02} are mostly damaged by the recombination centers H2 and H4. The defect H1 has a negligible effect on J_{02}, which can be attributed to its asymmetrical position

within the bandgap, combined with a low σ_p. Despite its apparent deep position in the bandgap, the defect H3 does not affect V_{OC} and J_{02}. Hence, it is possible that the defect presents a strong capture asymmetry resulting in a low minority-carrier capture cross section, or most likely, the energy level extracted from the trap signature is overestimated by the substantial effect of a temperature-dependent $\sigma_p(T)$. The latter theory is supported by experimental observations on some deep levels in III–V materials,[30] and also by some capture theories.[31]

According to Fig. 7, particles with higher relativistic mass are expected to damage V_{OC} and J_{02} more for a similar amount of 21 eV NIEL introduced in the cell, because these create a higher contribution of H2 and H4 defects. The best fit of the electron J_{02} data with $E_d = 35$ eV, as shown in Fig. 1, is thus in line with the E_d values found for H2 and H4. These defects cannot be formed by 0.5 MeV electrons, whose maximum energy transferable to a Ga or As atom is ~23 eV. The only defects that a 0.5 MeV electron can introduce in GaAs cells are H1 and H3, which exhibit a very low correlation coefficient with J_{02} according to the Pearson map in Fig. 8. The J_{02} degradation observed for 0.5 MeV electrons, shown in Fig. 1(c), can be only reconciled by postulating another recombination center characterized by $E_d < 23$ eV. This defect may be energetically located in the upper half of the bandgap out of the detectable range of admittance spectroscopy.

D. Proton–electron equivalence factors

Although the Pearson analysis yields a good correlation with $r = 0.8$ and 0.79 between the degradation of J_{02} and the concentration of the H2 and H4 defects, when these midgap defects are introduced by protons, the damage to J_{02} is more pronounced compared to the equivalent electron case, as shown in Figs. 1(c) and 1(d). A plausible explanation may be the presence of defects out of the detectable range with a different introduction rate for protons and electrons. Another possible reason could be ascribed to a different capture capability of the same midgap defects introduced by protons and electrons. The latter explanation can be rationalized to a certain degree with the help of the admittance
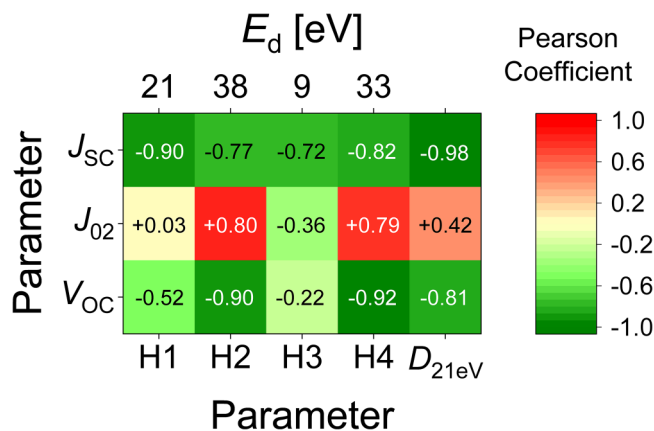

FIG. 8. Pearson's r correlation coefficients of the H1, H2, H3, H4 defect concentration and the DDD computed with $E_d = 21$ eV (D_{21eV}) over the solar cell J_{SC}, J_{02}, and V_{OC} remaining factors. A value of -1 expresses a good correlation for J_{SC} and V_{OC}, whereas $+1$ expresses a good correlation for J_{02}.
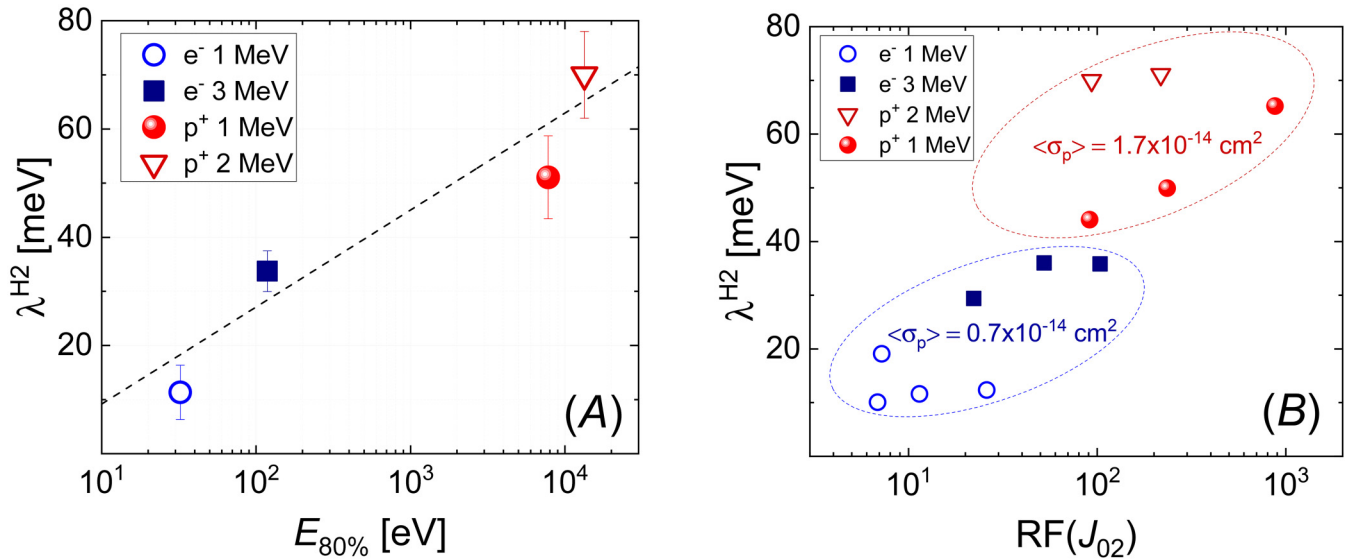
FIG. 9. (a) H2 distribution width λ^{H2} as a function of the recoil spectrum $E_{80\%}$ and (b) λ^{H2} as a function of the J_{02} remaining factor in irradiated GaAs component cells. The average capture cross section $<\sigma_p>$ for the proton- and electron-induced H2 defect is also reported.

spectroscopy results. Analyzing the H2 defect, the distribution width λ^{H2} is found to be not related to the DDD, but rather to the distribution of recoil energies. Using an 80% cutoff in the relative NIEL contribution plot in Fig. 4, the energy $E_{80\%}$ is determined. It represents the recoil energy up to which 80% of the total displacement damage of the incident particle is deposited. As illustrated in Fig. 9(a), a clear correlation is found between $E_{80\%}$ and λ^{H2}.

This is rationalized considering that higher $E_{80\%}$ values imply larger clusters of defects. The higher electronic disorder of these regions leads to a wide distribution of available energy levels within the bandgap, as already observed in the literature via DLTS in GaAs cells irradiated with neutrons[32] and protons.[33] Irradiated cells with higher λ^{H2} also exhibit a higher J_{02} remaining factor, as shown in Fig. 9(b). This suggests that the larger band tails around H2 may be linked to an increased capture capability of the defect in the SCR, thus affecting its damaging effectiveness with respect to J_{02}. In the limit of the uncertainty associated with the fitting of the admittance data, a higher σ_p is also observed for proton-irradiated cells compared to the electron case, which causes a slight blueshift of the H2 peak in the $-f\,dC/df$ plot of Fig. 3(a). This shows how a different particle recoil spectrum can impact the damaging effectiveness of a defect with respect to J_{02}. Although it might not be the only reason, this phenomenon can be linked to the existence of the electrical R_{ep} factor found for J_{02}. In the V_{OC} case, the existence of the R_{ep} factor is a direct consequence of the fact that for a moderately high dose level, V_{OC} is dominated by J_{02}.

VIII. CONCLUSION

In conclusion, temperature-dependent admittance spectroscopy was applied to the study of proton and electron radiation damage in GaAs component solar cells. With the help of a dedicated fitting routine, four majority carrier defects labeled H1–H4 were identified. The key benefit of admittance spectroscopy in contrast to analyzing macroscopic cell performance parameters is the fact that the radiation effects can be analyzed one step closer to the actual physical defect processes. The results depend to a lesser degree on the detailed electrical device design and thus can be interpreted more easily in terms of material-specific properties.

In particular, the combination of admittance spectroscopy with the NIEL fitting of the defect introduction rate was shown to result in a unique threshold energy for each of the defects, which provides additional insight into their crystallographic configuration. Moreover, it was established that a NIEL with a threshold energy of 21 eV accurately describes the scaling of the relative abundance of H1–H4 with the energy of the incident particle. For a given DDD, the relative fraction of high-energy defect increases with the relativistic mass of the incident particle.

A Pearson analysis was then used to link these results on a defect level to the degradation of the macroscopic cell parameters. The J_{SC} degradation shows a direct correlation with the combined H1–H4 DDD, analytically described by a threshold energy of 21 eV, from which a similar damaging effectiveness of each individual H1–H4 defect on J_{SC} can be concluded. For J_{02}, and thus also for V_{OC} at high doses, the energy level of the defect in the bandgap is important. Therefore, H2 and H4 play a major role for these parameters. This explains the fact that a threshold energy of 35 eV describes the DDD dependence of J_{02} very well, except for low-energy electrons. In addition, H2 was found to be more damaging if introduced by protons than by electrons. This behavior was traced back to a broader distribution of the H2 density of states in the bandgap in the proton case. It is in line with the existence of an R_{ep} factor for J_{02} and V_{OC} that corrects for the less damaging nature of electron DDD as compared to proton DDD.

ACKNOWLEDGMENTS

DATA AVAILABILITY

The data that support the findings of this study are available within the article.

REFERENCES

[1]S. R. Messenger, G. P. Summers, E. A. Burke, R. J. Walters, and M. A. Xapsos, "Modeling solar cell degradation in space: A comparison of the NRL displacement damage dose and the JPL equivalent fluence approaches," Prog. Photovoltaics Res. Appl. **9**, 103–121 (2001).

[2]A. Pillukat, K. Karsten, and P. Ehrhart, "Point defects and their reactions in e−-irradiated GaAs investigated by x-ray-diffraction methods," Phys. Rev. B **53**, 7823–7835 (1996).

[3]N. Chen, S. Gray, E. Hernandez-Rivera, D. Huang, P. D. LeVan, and F. Gao, "Computational simulation of threshold displacement energies of GaAs," J. Mater. Res. **32**, 1555–1562 (2017).

[4]ESA/ESTEC, ECSS-E-ST-20-08C Space Engineering—Photovoltaics Assemblies and Components (European Cooperation for Space Standardization, 2012), pp. 1–197.

[5]C. Baur, M. Gervasi, P. Nieminen, S. Pensotti, P. Rancoita, and M. Tacconi, "NIEL dose dependence for solar cells irradiated with electrons and protons," in Astroparticle, Particle, Space Physics and Detectors for Physics Applications (World Scientific, 2014), pp. 692–707.

[6]C. Pellegrino, A. Gagliardi, and C. G. Zimmermann, "Difference in space-charge recombination of proton and electron irradiated GaAs solar cells," Prog. Photovoltaics Res. Appl. **27**, 379–390 (2019).

[7]R. Campesato, C. Baur, M. Casale, M. Gervasi, E. Gombia, E. Greco, A. Kingma, P. G. Rancoita, D. Rozza, and M. Tacconi, "NIEL DOSE and DLTS analyses on triple and single junction solar cells irradiated with electrons and protons," in 2018 IEEE 7th World Conference on Photovoltaic Energy Conversion (WCPEC) (A Joint Conference of 45th IEEE PVSC, 28th PVSEC & 34th EU PVSEC) (IEEE, 2018), pp. 3768–3772.

[8]T. P. Weiss, A. Redinger, D. Regesch, M. Mousel, and S. Siebentritt, "Direct evaluation of defect distributions from admittance spectroscopy," IEEE J. Photovoltaics **4**, 1665–1670 (2014).

[9]A. I. Baranov, A. S. Gudovskikh, D. A. Kudryashov, A. A. Lazarenko, I. A. Morozov, A. M. Mozharov, E. V. Nikitina, E. V. Pirogov, M. S. Sobolev, K. S. Zelentsov, A. Y. Egorov, A. Darga, S. Le Gall, and J.-P. Kleider, "Defect properties of InGaAsN layers grown as sub-monolayer digital alloys by molecular beam epitaxy," J. Appl. Phys. **123**, 161418 (2018).

[10]M. Levinshtein, S. Rumyantsev, and M. Shur, Handbook Series on Semiconductor Parameters (World Scientific, 1996), Vol. 2.

[11]P. Blood and J. W. Orton, The Electrical Characterization of Semiconductors: Majority Carriers and Electron States, 1st ed. (Academic Press, New York, 1992).

[12]R. Hoheisel and A. W. Bett, "Experimental analysis of majority carrier transport processes at heterointerfaces in photovoltaic devices," IEEE J. Photovoltaics **2**, 398–402 (2012).

[13]M. Burgelman, P. Nollet, and S. Degrave, "Modelling polycrystalline semiconductor solar cells," Thin Solid Films **361–362**, 527–532 (2000).

[14]W. Hu, J. Xie, H. W. Chau, and B. C. Si, "Evaluation of parameter uncertainties in nonlinear regression using microsoft excel spreadsheet," Environ. Syst. Res. **4**, 4 (2015).

[15]I. Jun, "Effects of secondary particles on the total dose and the displacement damage in space proton environments," IEEE Trans. Nucl. Sci. **48**, 162–175 (2001).

[16]J. Lindhard, V. Nielsen, M. Scharff, and P. V. Thomsen, "Integral equations governing radiation effects," Mat. Fys. Medd. Dan. Vid. Selsk. **33**(10), 1–41 (1963).

[17]M. J. Boschini, C. Consolandi, M. Gervasi, S. Giani, D. Grandi, V. Ivanchenko, P. Nieminem, S. Pensotti, P. G. Rancoita, and M. Tacconi, "Nuclear and non-ionizing energy-loss of electrons with low and relativistic energies in materials and space environment," arXiv:1111.4042 (2012), pp. 961–982.

[18]M. J. Boschini, C. Consolandi, M. Gervasi, S. Giani, D. Grandi, V. Ivanchenko, P. Nieminem, S. Pensotti, P. G. Rancoita, and M. Tacconi, "An expression for the Mott cross section of electrons and positrons on nuclei with Z up to 118," Radiat. Phys. Chem. **90**, 39–66 (2013).

[19]M. Boschini, C. Consolandi, M. Gervasi, S. Giani, D. Grandi, V. Ivanchenko, S. Pensotti, P. Rancoita, and M. Tacconi, "Nuclear and non-ionizing energy-loss for coulomb scattered particles from low energy up to relativistic regime in space radiation environment," in Cosmic Rays for Particle and Astroparticle Physics (World Scientific, 2011), pp. 9–23.

[20]M. Boschini, P. Rancoita, and M. Tacconi, see http://www.sr-niel.org/ for "SR-NIEL calculator: Screened relativistic (SR) treatment for calculating the displacement damage and nuclear stopping powers for electrons, protons, light- and heavy-ions in materials," available at INFN sez. Milano-Bicocca, Italy (last accessed July 2020).

[21]F. Gao, N. Chen, E. Hernandez-Rivera, D. Huang, and P. D. LeVan, "Displacement damage and predicted non-ionizing energy loss in GaAs," J. Appl. Phys. **121**, 095104 (2017).

[22]J. F. Ziegler, M. D. Ziegler, and J. P. Biersack, "SRIM—The stopping and range of ions in matter (2010)," Nucl. Instrum. Methods Phys. Res. Sect. B **268**, 1818–1823 (2010).

[23]T. Mattila and R. M. Nieminen, "Direct antisite formation in electron irradiation of GaAs," Phys. Rev. Lett. **74**, 2721–2724 (1995).

[24]J. C. Bourgoin, H. J. von Bardeleben, and D. Stiévenard, "Native defects in gallium arsenide," J. Appl. Phys. **64**, R65–R92 (1988).

[25]J. C. Bourgoin and M. Zazoui, "Irradiation-induced degradation in solar cell: Characterization of recombination centres," Semicond. Sci. Technol. **17**, 453–460 (2002).

[26]H. J. von Bardeleben, D. Stiévenard, D. Deresmes, A. Huber, and J. C. Bourgoin, "Identification of a defect in a semiconductor: EL2 in GaAs," Phys. Rev. B **34**, 7192–7202 (1986).

[27]D. Stievenard, X. Boddaert, and J. C. Bourgoin, "Irradiation-induced defects in p-type GaAs," Phys. Rev. B **34**, 4048–4058 (1986).

[28]D. Pons and J. C. Bourgoin, "Irradiation-induced defects in GaAs," J. Phys. C Solid State Phys. **18**, 3839–3871 (1985).

[29]A. F. Wright and N. A. Modine, "Migration processes of the As interstitial in GaAs," J. Appl. Phys. **120**, 215705 (2016).

[30]P. Blood and J. J. Harris, "Deep states in GaAs grown by molecular beam epitaxy," J. Appl. Phys. **56**, 993–1007 (1984).

[31]J. Bourgoin and M. Lannoo, Point Defects in Semiconductors II, Springer Series in Solid-State Sciences Vol. 35 (Springer, Berlin, 1983).

[32]R. M. Fleming, D. V. Lang, C. H. Seager, E. Bielejec, G. A. Patrizi, and J. M. Campbell, "Continuous distribution of defect states and band gap narrowing in neutron irradiated GaAs," J. Appl. Phys. **107**, 123710 (2010).

[33]J. H. Warner, S. R. Messenger, R. J. Walters, S. A. Ringel, and M. R. Brenner, "A deep level transient spectroscopy study of electron and proton irradiated p+n GaAs diodes," in Proceedings of the European Conference on Radiation and its Effects on Components and Systems (IEEE, 2009), Vol. 57, pp. 282–285.